Heliyon 9 (2023) e18374

Contents lists available at ScienceDirect

Heliyon

journal homepage: www.cell.com/heliyon

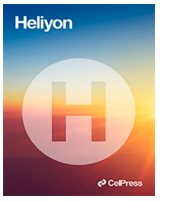

Beam intensity and spectral coherence of Hermite-cosine-Gaussian rectangular multi-Gaussian correlated Schell-model beam in oceanic turbulence

Xu Wu [a,*], Chuang Wang [a], Yuhui Kong [a], Kenan Wu [b,**]

[a] Information Science and Technology College, Dalian Maritime University, Linghai Road 1, Dalian, 116026, China
[b] Key Laboratory of Chemical Lasers, Dalian Institute of Chemical Physics, Chinese Academy of Sciences, Zhongshan Road 457, Dalian, 116023, China

ARTICLE INFO

Keywords:
Oceanic turbulence
Hermite-cosine-Gaussian rectangular multi-Gaussian correlation Schell-model beam
Laser propagation

ABSTRACT

The beam spreading and evolution behavior of a partially coherent, Hermite-cosine-Gaussian (HcosG) rectangular multi-Gaussian correlated Schell-model beam propagating in oceanic turbulence is studied. Analytical expressions for the cross-spectral density function, as well as the root mean square (rms) beam width and the spectral degree of coherence, are derived based on the extended Huygens-Fresnel principle. The HcosG rectangular multi-Gaussian correlated Schell-model beam exhibits a multi-lobe pattern at short propagation distances. The dependencies of the number, size, shape, and centroid of the lobes on displacement parameters, source size, order of field distribution, and displacement are investigated. As the propagation distance increases, the spectral coherence decreases, and the differences between the spectral coherence curves gradually diminish. Additionally, for HcosG rectangular multi-Gaussian correlated Schell-model beams, better propagation performance was found in oceanic turbulence with larger mean square temperature dissipation rate, smaller turbulent kinetic energy dissipation rate per unit mass of fluid, and larger relative strength of temperature and salinity fluctuation.

1. Introduction

In recent years, the rapid development of marine communication in the military, fishery, detection, and other fields has sparked great interest in the propagation characteristics of beams in ocean turbulence [1]. Research in this area can be helpful for the application and development of remote sensing, imaging, optical communication, and other technologies in the marine field [2]. Numerous beams have been extensively studied: such as Gaussian Schell-model vortex beams [3], partially coherent Lorentz-Gauss beams [4], and partially coherent radially polarized doughnuts [5], among others.

Besides the aforementioned beam models, the Hermite-sinusoidal-Gaussian beam also attracts a lot of attention. The Hermite-sinusoidal-Gaussian beams, introduced by Casperson and Tovar in 1998, are a kind of general solution of the paraxial wave equation [6,7]. Since then, numerous authors have analyzed these beams, including studies on the propagation of Hermite-cosh-Gaussian laser beams in atmospheric turbulence [8], and investigations into Hermite-cosine-Gaussian beams in uniaxial crystals orthogonal to

* Corresponding author.
** Corresponding author.
E-mail addresses: xuwu@dlmu.edu.cn (X. Wu), wukn@dicp.ac.cn (K. Wu).

https://doi.org/10.1016/j.heliyon.2023.e18374
Received 11 March 2023; Received in revised form 14 July 2023; Accepted 14 July 2023
Available online 19 July 2023

the optical axis [9], through atmospheric turbulence [10], and ABCD optical systems with or without apertures have been examined [11]. The vectorial structure and the energy flux distribution of HcosG beams in the far field have also been studied [12]. It has also been shown that the HcosG beams could be used to realize soliton in nonlinear medium [13]. The HcosG beams have rich structure and controllable morphology, and can be used as multi-dimensional information carrier [14]. Previous works have shown the possibility to capture more power remotely by using higher-mode-indexed HcosG beams, making these beams promising in communication and directed energy applications [15,16]. However, the propagation characteristics of Hermite-cosine-Gaussian beams in ocean turbulence have not yet been reported [17]. Compared with fully coherent beams, partially coherent beams exhibit better resistance to turbulence [18], while those with non-conventional correlation functions can generate specific far-zone spatial intensity distribution [19]. Specifically, the far-field intensity pattern of a rectangular multi-Gaussian Schell-model (RMGSM) beam has rectangular flat-top shape with adjustable edge sharpness and is shape-invariant throughout the far field [20]. This makes HcosG beams with rectangular multi-Gaussian Schell-model a desirable signal source in data transfer and sensing applications [21].

The propagation of Hermite-cosine-Gaussian rectangular multi-Gaussian correlated Schell-model beam in ocean turbulence is studied in this paper. In Sec. 2, the analytical formulas of cross-spectral density, root mean square beam width, and spectral coherence are derived. In Sec. 3, the propagation characteristics and spectral characteristics of the beam are evaluated with different initial beam parameters and oceanic turbulence parameters. Finally, conclusions are drawn in Sec. 4.

2. Propagation theory

The field of HcosG rectangular multi-Gaussian correlated Schell-model beam at the source plane z = 0 is [8,22,23]:

$$\begin{aligned} E(\rho,0) &= E(\rho_x,\rho_y,0) \\ &= 0.5A_c H_n(a_x\rho_x+b_x)H_m(a_y\rho_y+b_y)\exp\left[-0.5\left(\rho_x^2/\alpha_{sx}^2+\rho_y^2/\alpha_{sy}^2\right)\right] \\ &\quad\times\left\{\exp\left[i\left(V_{xr}\rho_x+V_{yr}\rho_y\right)\right]+\exp\left[-i\left(V_{xr}\rho_x+V_{yr}\rho_y\right)\right]\right\}, \end{aligned} \tag{1}$$

where $\rho = (\rho_x, \rho_y)$ is the coordinate vector in the source plane, A_c is the amplitude parameter, α_{sx} and α_{sy} are the waist of the Gaussian beam, and V_{xr}, V_{yr} are the complex displacement parameters of the Gaussian part. $H_n()$ is the Hermite polynomial of order n [24]. a_x and a_y are width parameters, while b_x and b_y are displacement parameters.

The partially coherent cross-spectral density function of the beam source can be expressed as [25]:

$$\begin{aligned} W(\rho_1,\rho_2,0) &= \langle E(\rho_1,0)E^*(\rho_2,0)\rangle \\ &= \sqrt{I(\rho_1,0)I(\rho_2,0)}\,g(\rho_{1x}-\rho_{2x},\rho_{1y}-\rho_{2y}). \end{aligned} \tag{2}$$

Here $g(\rho_{1x}-\rho_{2x},\rho_{1y}-\rho_{2y})$ is the spectral coherence degree, expressed as Eq. (3) [26]:

$$\begin{aligned} g(\rho_{1x}-\rho_{2x},\rho_{1y}-\rho_{2y}) &= \frac{1}{C^2}\sum_{m_x=1}^{M}\frac{(-1)^{m_x-1}}{\sqrt{m_x}}\binom{M}{m_x}\exp\left[-\frac{(\rho_{1x}-\rho_{2x})^2}{2m_x\delta_x^2}\right] \\ &\quad\times\sum_{m_y=1}^{M}\frac{(-1)^{m_y-1}}{\sqrt{m_y}}\binom{M}{m_y}\exp\left[-\frac{(\rho_{1y}-\rho_{2y})^2}{2m_y\delta_y^2}\right], \end{aligned} \tag{3}$$

where $C=\sum_{m=1}^{M}\binom{M}{m}\frac{(-1)^{m-1}}{\sqrt{m}}$ is the normalization factor and $\binom{M}{m}$ is the binomial coefficient. In addition, δ_x and δ_y denote the spatial coherence lengths in the x and y directions, respectively.

By substituting Eq. (1) into Eq. (2), HcosG rectangular multi-Gaussian correlated Schell-model beam at the source plane can be expressed as Eq. (4):

$$\begin{aligned} W(\rho_1,\rho_2,0) &= H_n(a_x\rho_{1x}+b_x)H_m(a_y\rho_{1y}+b_y)\exp\left[-0.5\left(\rho_{1x}^2/\alpha_{sx}^2+\rho_{1y}^2/\alpha_{sy}^2\right)\right] \\ &\quad\times H_n(a_x\rho_{2x}+b_x)H_m(a_y\rho_{2y}+b_y)\exp\left[-0.5\left(\rho_{2x}^2/\alpha_{sx}^2+\rho_{2y}^2/\alpha_{sy}^2\right)\right] \\ &\quad\times\cos\left(V_{xr}\rho_{1x}+V_{yr}\rho_{1y}\right)\cos\left(V_{xr}\rho_{2x}+V_{yr}\rho_{2y}\right) \\ &\quad\times\frac{1}{C^2}\sum_{m_x=1}^{M}\frac{(-1)^{m_x-1}}{\sqrt{m_x}}\binom{M}{m_x}\exp\left[-\frac{(\rho_{1x}-\rho_{2x})^2}{2m_x\delta_x^2}\right] \\ &\quad\times\sum_{m_y=1}^{M}\frac{(-1)^{m_y-1}}{\sqrt{m_y}}\binom{M}{m_y}\exp\left[-\frac{(\rho_{1y}-\rho_{2y})^2}{2m_y\delta_y^2}\right]. \end{aligned} \tag{4}$$

According to the extended Huygens-Fresnel principle, the cross-spectral density function of laser beam in ocean turbulence can be obtained as follows [27]:

$$W(r_1,r_2,z=L)=\left(\frac{k}{2\pi z}\right)^2\iint d^2\rho_1\iint d^2\rho_2 W(\rho_1,\rho_2,0)\times\exp\left\{-\frac{ik}{2z}\left[(r_1-\rho_1)^2-(r_2-\rho_2)^2\right]\right\}\times\langle\exp[\psi^*(r_1,\rho_1)+\psi(r_2,\rho_2)]\rangle, \tag{5}$$

where $r_1=(r_{1x},r_{1y})$ and $r_2=(r_{2x},r_{2y})$ denote the transverse position vectors in the receiving planes, k is the wavenumber, and $\psi^*(r_1,\rho_1)$ is a random part of complex phase of spherical wave caused by ocean turbulence. The quadratic approximation of the Rytov wave phase structure function can be written as [28,29]:

$$\langle\exp[\psi^*(r_1,\rho_1)+\psi(r_2,\rho_2)]\rangle=\exp\left\{-\frac{1}{\rho_0{}^2}\left[(\rho_1-\rho_2)^2+(\rho_1-\rho_2)(r_1-r_2)+(r_1-r_2)^2\right]\right\}, \tag{6}$$

where $\rho_0=[\pi^2k^2z/3\int_0^\infty\kappa^3\varphi_{ocean}(\kappa)d\kappa]^{-1/2}$ is the spatial coherence radius of a spherical wave propagated through turbulence [30]. $\varphi_{ocean}(\kappa)$ is the spatial power spectrum of refractive index fluctuation of ocean turbulence, expressed as Eq. (7) [4]:

$$\varphi_{ocean}(\kappa)=0.388\times10^{-8}\chi_T\varepsilon^{-1/3}\kappa^{-11/3}\left[1+2.35(\kappa\eta)^{2/3}\right]\times\frac{\chi_T}{\varsigma^2}\left[\varsigma^2\exp(-A_T\delta)+\exp(-A_S\delta)-2\varsigma\exp(-A_{TS}\delta)\right], \tag{7}$$

where κ is the spatial wavenumber of refractive index fluctuation, χ_T is the dissipation rate of the mean square temperature, ε is the turbulent kinetic energy dissipation rate, η is the Kolmogorov scale, $A_T=1.863\times10^{-2}$, $A_S=1.9\times10^{-4}$, $A_{TS}=9.41\times10^{-3}$, $\delta=8.284(\kappa\eta)^{4/3}+12.978(\kappa\eta)^2$, and ς is the equilibrium parameter describing the relative intensity of temperature and salinity fluctuations [31].

By substituting Eq. (6) into Eq. (5) for integral calculation, we can obtain

$$\begin{aligned}W(r_1,r_2,z)&=\left(\frac{\pi k}{4C\pi z}\right)^2\exp\left[-\lambda\left(r_1{}^2-r_2{}^2\right)-P(r_1-r_2)^2\right]\\&\times\left\{S_{x1}S_{y1}\exp\left\{\frac{f_1{}^2}{4(\beta_1+\lambda)}+\frac{[f_1\varsigma_x+2f_2(\beta_1+\lambda)]^2}{C_{x2}}+\frac{f_3{}^2}{4(\beta_2+\lambda)}+\frac{\left[f_3\varsigma_y+2f_4(\beta_2+\lambda)\right]^2}{C_{y2}}\right\}\right.\\&+S_{x2}S_{y2}\exp\left\{\frac{f_5{}^2}{4(\beta_1+\lambda)}+\frac{[f_5\varsigma_x+2f_6(\beta_1+\lambda)]^2}{C_{x2}}\frac{f_7{}^2}{4(\beta_2+\lambda)}+\frac{\left[f_7\varsigma_y+2f_8(\beta_2+\lambda)\right]^2}{C_{y2}}\right\}\\&+S_{x3}S_{y3}\exp\left\{\frac{f_9{}^2}{4(\beta_1+\lambda)}+\frac{[f_9\varsigma_x+2f_{10}(\beta_1+\lambda)]^2}{C_{x2}}\frac{f_{11}{}^2}{4(\beta_2+\lambda)}+\frac{\left[f_{11}\varsigma_y+2f_{12}(\beta_2+\lambda)\right]^2}{C_{y2}}\right\}\\&\left.+S_{x4}S_{y4}\exp\left\{\frac{f_{13}{}^2}{4(\beta_1+\lambda)}+\frac{[f_{13}\varsigma_x+2f_{14}(\beta_1+\lambda)]^2}{C_{x2}}+\frac{f_{15}{}^2}{4(\beta_2+\lambda)}+\frac{\left[f_{15}\varsigma_y+2f_{16}(\beta_2+\lambda)\right]^2}{C_{y2}}\right\}\right\},\end{aligned} \tag{8}$$

where

$$\begin{aligned}S_{x1}=&\sum_{l_{x1}=0}^{n/2}\sum_{l_{nx1}=0}^{n-2l_{x1}}\sum_{k_{x1}=0}^{l_{nx1}/2}\sum_{l_{nx11}=0}^{l_{nx1}-2k_{x1}}\sum_{l_{x2}=0}^{n/2}\sum_{l_{nx2}=0}^{n-2l_{x2}}\sum_{k_{x2}=0}^{(l_{nx11}+l_{nx2})/2}(-1)^{l_{x1}+l_{x2}}2^{2n-2l_{x1}-2k_{x2}-l_{nx1}-l_{nx2}-l_{nx11}}\\&\times a_x{}^{l_{nx1}+l_{nx2}}b_x{}^{2n-2l_{x1}-2k_{x2}-l_{nx1}-l_{nx2}}(\beta_1+\lambda)^{-0.5-l_{nx1}+2k_{x1}}T_{lx1}T_{lx2}\\&\times\binom{n}{2l_{x1}}\binom{n}{2l_{x2}}\binom{n-2l_{x1}}{l_{nx1}}\binom{l_{nx1}-2k_{x1}}{l_{nx11}}\binom{n-2l_{x2}}{l_{nx2}}\\&\times\frac{l_{nx1}!}{k_{x1}!(l_{x1}-2k_{x1})!}\frac{(l_{nx11}+l_{nx2})}{k_{x2}!(l_{nx11}+l_{nx2}-2k_{x2})}\\&\times f_1{}^{l_{nx1}-2k_{x1}-l_{nx11}}\varsigma_x{}^{l_{nx11}}\left[\frac{4\left(\beta_1{}^2-\lambda^2\right)-\varsigma_x{}^2}{4(\beta_1+\lambda)}\right]^{-0.5-0.5(l_{nx11}+l_{nx2}-2k_{x2})}\\&\left\{\frac{f_1\varsigma_x+2f_2(\beta_1+\lambda)}{C_{x1}}\right\}^{l_{nx11}+l_{nx2}-2k_{x2}},\end{aligned} \tag{9}$$

with $f_1=\frac{ikr_{1x}}{z}+\frac{1}{\rho_0{}^2}(-r_{1x}+r_{2x})+iV_{xr}$, $f_2=\frac{ikr_{2x}}{z}+\frac{1}{\rho_0{}^2}(r_{1x}-r_{2x})+iV_{xr}$, $f_3=\frac{ikr_{1y}}{z}+\frac{1}{\rho_0{}^2}(-r_{1y}+r_{2y})+iV_{yr}$, $f_4=\frac{ikr_{2y}}{z}+\frac{1}{\rho_0{}^2}(r_{1y}-r_{2y})+iV_{yr}$, $C_{x1}=(\beta_1+\lambda)^{0.5}[(\beta_1{}^2+\lambda^2)-\varsigma_x{}^2]^{0.5}$, $C_{y1}=(\beta_2+\lambda)^{0.5}[(\beta_2{}^2+\lambda^2)-\varsigma_y{}^2]^{0.5}$, $C_{x2}=4(\beta_1+\lambda)[4(\beta_1{}^2-\lambda^2)-\varsigma_x{}^2]$, $C_{y2}=4(\beta_2+\lambda)[4(\beta_2{}^2-\lambda^2)-\varsigma_y{}^2]$, $\beta_1=\frac{1}{2\alpha_x^2}+\frac{1}{2m_x\delta_x^2}+\frac{1}{\rho_0{}^2}$, $\beta_2=\frac{1}{2\alpha_y^2}+\frac{1}{2m_y\delta_y^2}+\frac{1}{\rho_0{}^2}$, $\varsigma_x=\frac{1}{m_x\delta_x{}^2}+\frac{2}{\rho_0{}^2}$, $\lambda=\frac{ik}{2z}$, and $T_{lxi}=1\times3\times\ldots(2l_{xi}-1), i=1,2$. The expressions of S_{x2}, S_{x3}, and S_{x4} are obtained by changing the plus or minus sign before V_{xr} in S_{x1}. S_{y1}, S_{y2}, S_{y3}, and S_{y4} are obtained by replacing all x

indices in the sum equation of S_{x1}, S_{x2}, S_{x3}, and S_{x4} with y indices and n with m.

Eqs. (8) and (9) provide an analytical expression for the cross-spectral density function of HcosG rectangular multi-Gaussian correlated Schell-model beam propagation in ocean turbulence. By setting $r_1 = r_2$, the average intensity can be obtained as Eq. (10) [32]:

$$I(r,z) = W(r,r,z). \tag{10}$$

The root means square (rms) beam width [33] and the spectral coherence [25] can be obtained from Eq. (11)

$$Wlt(z) = \sqrt{\frac{\iint \mathrm{r}^2 \mathrm{I}(\mathrm{r},\mathrm{z})\mathrm{d}^2\mathrm{r}}{\iint \mathrm{I}(\mathrm{r},\mathrm{z})\mathrm{d}^2\mathrm{r}}}, \tag{11}$$

and Eq. (12)

$$\mu(r_1,r_2,z) = \frac{W(r_1,r_2,z)}{[W(r_1,r_1,z)W(r_2,r_2,z)]^{\frac{1}{2}}}, \tag{12}$$

respectively.

3. Numerical examples and analysis

In this section, the average intensity and coherence characteristics of HcosG rectangular multi-Gaussian correlation Schell-model beams propagating in ocean turbulence are studied by numerical examples. The calculation parameters were set as, $\lambda = 532nm$, $\varsigma = -2.5$, $\chi_T = 10^{-8}K^2s^{-1}$, $\varepsilon = 10^{-7}m^2s^{-3}$, unless otherwise specified.

Fig. 1 displays the normalized average intensity of a Hermite-cosine-Gaussian rectangular multi-Gaussian correlated Schell-model beam with $m = 1$ and $n = 1$ propagating through free space and oceanic turbulence. The average intensity undergoes various stages of evolution as it propagates. As the beams propagate through the oceanic turbulence, between propagation distances of approximately 10 m–80 m, the sidelobe profile gradually shifts towards the center. Additionally, the sidelobe profile transitions from the three-lobe profile to the single-lobe profile. When z = 80 m, the image changes to a four-lobe profile. The dark hollow center of the Hermite-cosine-Gaussian rectangular multi-Gaussian correlated Schell-model beam shrinks due to the expansion of each petal as z increases. At a propagation distance of about 100 m–200 m, the beam evolves from a four-lobe profile to a single-lobe Gaussian-like beam. The beam continues to maintain a single-lobe profile as z increases further. Finally, the normalized intensity value in Fig. 1(e)-1(h) demonstrate that when z = 10 m, the maximum normalized intensity is 0.98. However, as z increases to 200 m, the normalized intensity value decreases significantly to about 0.082. This decline in normalized intensity value occurs due to the diffusion of the petal contour with increasing propagation distance z. Compared with beam propagation in free space (Fig. 1(a)-1(d)), the four-lobe beam shrinks faster in oceanic turbulence with the same propagation distance, and the maximum normalized intensity is also larger.

In Fig. 2, the normalized average intensity of a Hermite-cosine-Gaussian rectangular multi-Gaussian correlated Schell-model beam is presented for various values of m and n. This figure highlights the fact that the difference in the values of m and n results in changes in the number of lobes. As depicted in Fig. 2(e)-2(h), the number of lobes in the normalized intensity figure varies between single lobe,

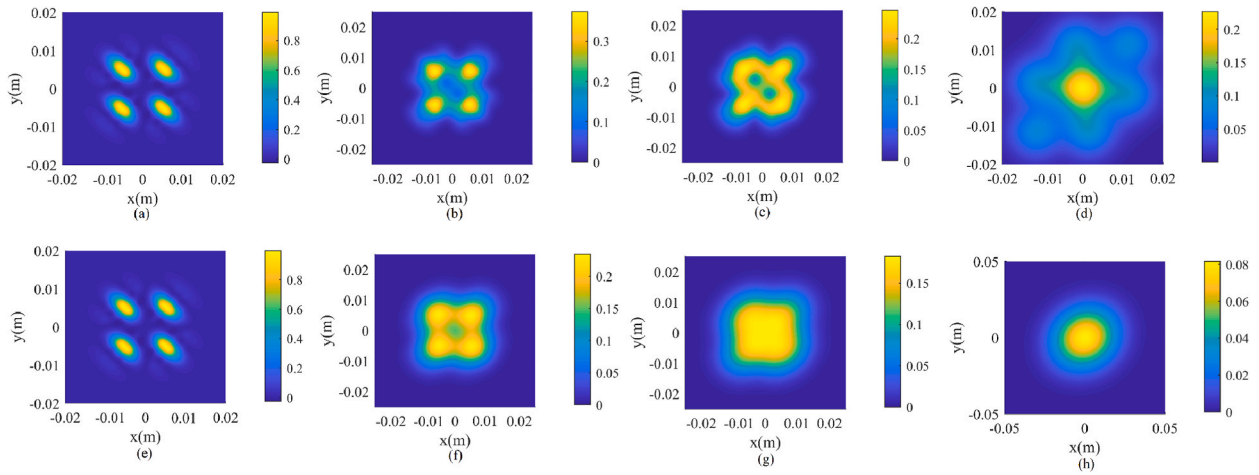

Fig. 1. Evolution of normalized intensity distribution of the Hermite-cosine-Gaussian rectangular multi-Gaussian correlated Schell-model beam in (a–d) free space and (e–h) turbulent oceanic conditions at various distances from the source: (a, e) z = 10 m, (b, f) z = 80 m, (c, g) z = 100 m, (d, h) z = 200 m. It is noteworthy that all the intensity data presented have been normalized with respect to the initial wave's peak intensity value at z = 0 m.

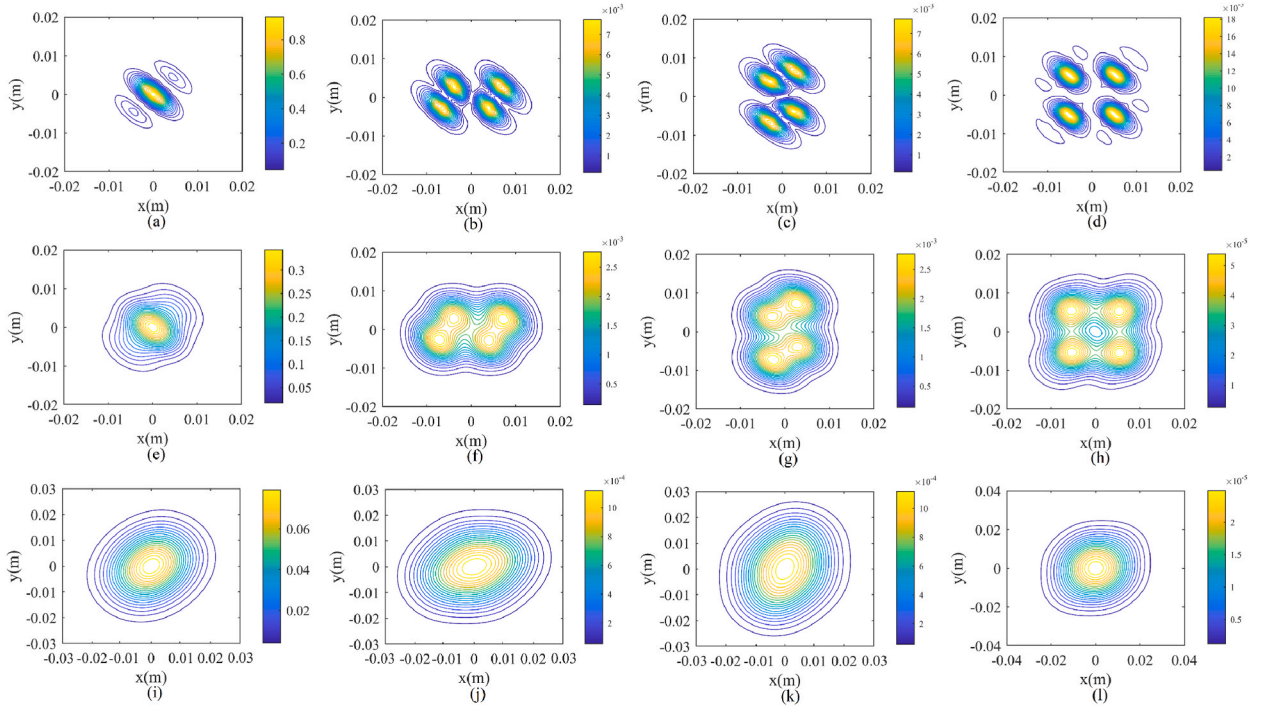

Fig. 2. Normalized intensity distribution of the Hermite-cosine-Gaussian rectangular multi-Gaussian correlated Schell-model beam in turbulent oceanic conditions for various orders of the field distribution denoted by indices n and m: (a, e, i) n = 0, m = 0, (b, f, j) n = 1, m = 0, (c, g, k) n = 0, m = 1, (d, h, l) n = 1, m = 1, where (a–d) are at z = 10 m, (e–h) are at z = 70 m, and (i–l) are at z = 150 m. It is noteworthy that all the intensity data presented have been normalized with respect to the initial wave's peak intensity value at z = 0 m.

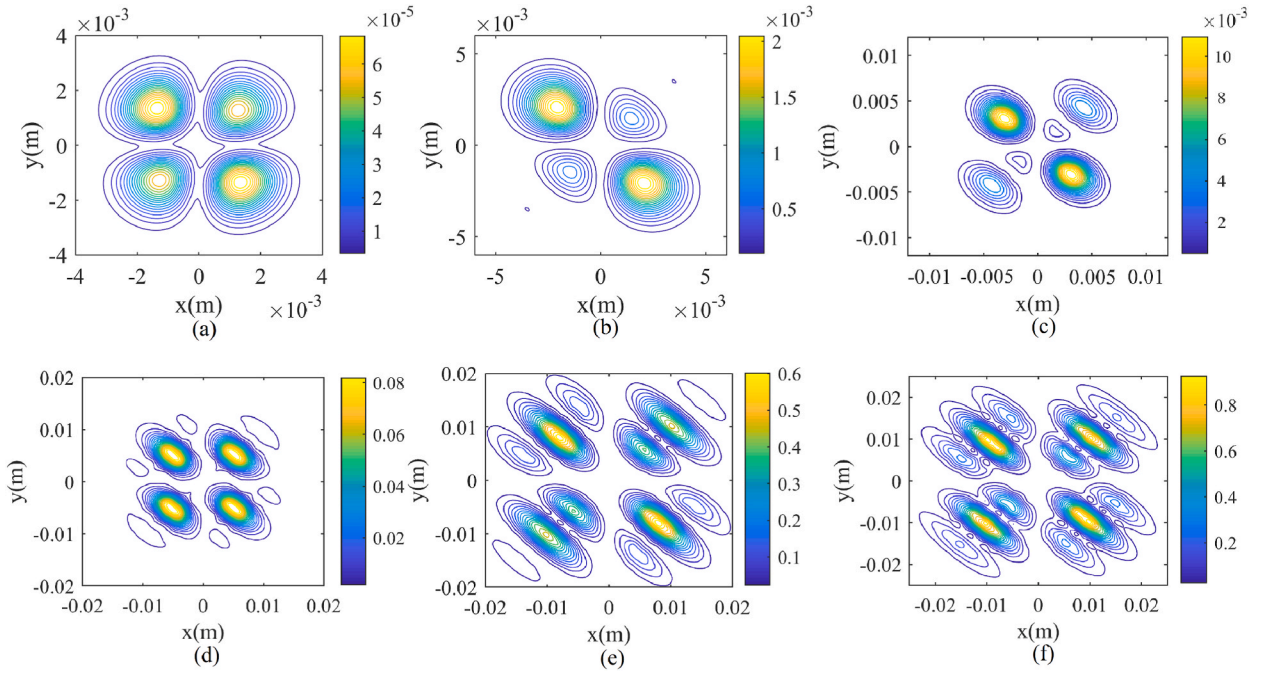

Fig. 3. Normalized intensity distribution of the Hermite-cosine-Gaussian rectangular multi-Gaussian correlated Schell-model beam in turbulent oceanic conditions with n = 1 and m = 1. Specifically, (a) $\alpha_{sx} = \alpha_{sy} = 0.001$ m, (b) $\alpha_{sx} = \alpha_{sy} = 0.002$ m, (c) $\alpha_{sx} = \alpha_{sy} = 0.003$ m, (d) $\alpha_{sx} = \alpha_{sy} = 0.005$ m, (e) $\alpha_{sx} = \alpha_{sy} = 0.008$ m, (f) $\alpha_{sx} = \alpha_{sy} = 0.009$ m.

double lobe, and four lobes, respectively. Notably, changing m and n does not affect the symmetry of Fig. 2(a)-2(d), which remains central symmetry. However, differences between m and n result in changes in the relative orientation of the lobes. For instance, Fig. 2 (b) exhibits two double-lobe contours located at the left and right sides of the figure, while Fig. 2(c) shows two double-lobe contours positioned at the upper and lower sides of figure. It should be emphasized that the normalized intensity of the Hermite-cosine-Gaussian rectangular multi-Gaussian correlated Schell-model beam decreases as the values of n and m increase. For example, the maximum normalized intensity of Fig. 2(l) is 2.5×10^{-5}, while that of Fig. 2(i) is 0.08. Additionally, as the propagation distance z varies, the number of lobes decreases, and the multi-lobe profile gradually merges into a single lobe and the beam profile diffuses accordingly. In Fig. 2(i)-2(l), it can be observed that all the beams with different values of m and n evolve into Gaussian-like beams in the far field. Moreover, the variation of m and n affects the spreading velocity of the quasi-Gaussian beams in the x and y directions. The larger the values of m and n, the faster the spots spread. When m and n are not equal, the diffusion velocity in the x and y directions is different, and the spot becomes elliptical.

Fig. 3 depicts the normalized average intensity of the Hermite-cosine-Gaussian rectangular multi-Gaussian correlated Schell-model beam in ocean turbulence with different parameters of α_{sx} and α_{sy}. The lobes shown in Fig. 3(a)-3(f) are centrosymmetric, and their normalized intensity increases as α_{sx} and α_{sy} increase. When $\alpha_{sx} = \alpha_{sy} = 0.001$ m, the maximum normalized intensity is 7.08×10^{-5}, whereas when $\alpha_{sx} = \alpha_{sy} = 0.009$ m, the maximum normalized intensity is 0.97. Furthermore, changing the values of α_{sx} and α_{sy} affect the number of lobes and the size of lobe profiles. Fig. 3(a)-3(c) display a single four-lobe profile, whereas with the increase of α_{sx} and α_{sy}, the difference between the lobe energy on the main diagonal and the lobe energy on the sub-diagonal also gradually increases. Fig. 3(c)-3(f) exhibit beam patterns with four sidelobe contours. As α_{sx} and α_{sy} increase, the sidelobe contours separate from the single-lobe contours into three-lobe contours. It can be observed from the figure that the smaller the values of α_{sx} and α_{sy}, the faster the sidelobe fusion into a single lobe of the normalized intensity profile will occur.

Fig. 4 illustrates the influence of Gaussian shift parameters on the propagation characteristics of Hermite-Cosine-Gaussian rectangular multi-Gaussian correlated Schell-model beams in oceanic turbulence when $n = 1$ and $m = 0$. Initially, different values of V_{xr} affect the number and shape of lobes. As shown in Fig. 4(a)-4(d), increasing V_{xr} results in the appearance of two regular single-lobe contours in Fig. 4(a), a transition from a regular to a distorted shape in Fig. 4(b), and the formation of two double-lobe contours in Fig. 4(c) and (d), respectively. The maximum normalization values in Fig. 4(a)-4(d) are 0.96, 0.81, 0.64, and 0.56, respectively. Therefore, by adjusting the amplitudes of V_{xr} and V_{yr}, the number of near-field cosine oscillations (lobes) can be changed. The higher the amplitudes of V_{xr} and V_{yr}, the more cosine oscillations (lobes) will be generated, and the normalized intensity value decreases with the increase of V_{xr}. Additionally, it can be observed in Fig. 4(e)-4(h) that as the propagation distance z increases, the lobes tend to merge.

Fig. 5 examines the impact of Hermite polynomial displacement parameters b_x and b_y on the propagation characteristics of the Hermite-cosine-Gaussian rectangular multi-Gaussian correlated Schell-model beam in oceanic turbulence. As shown in Fig. 5(a)-5(d) and Fig. 5(e)-5(h), increasing the value of b_x leads to energy transfer between sidelobes, change in the number of lobes, break in symmetry, and increase in normalized intensity. Fig. 5(a) displays two double-lobes with central symmetry. In Fig. 5(c), energy transfer occurs, symmetry is broken, and the left sidelobe gradually disappears, while the right sidelobe remains double-lobe. In Fig. 5 (d), the left sidelobe almost vanishes, and energy is transferred to the right sidelobe. At b_x values of 0, 0.2, 0.5, and 1, the maximum normalized intensity is 0.13, 0.22, 0.42, and 0.96, respectively. Thus, adjusting the value of b_x can alter the maximum normalized value of the transmitted beam within a certain distance range and cause a displacement of the beam's centroid.

The normalized average intensity of the Hermite-cosine-Gaussian rectangular multi-Gaussian correlated Schell-model beam is

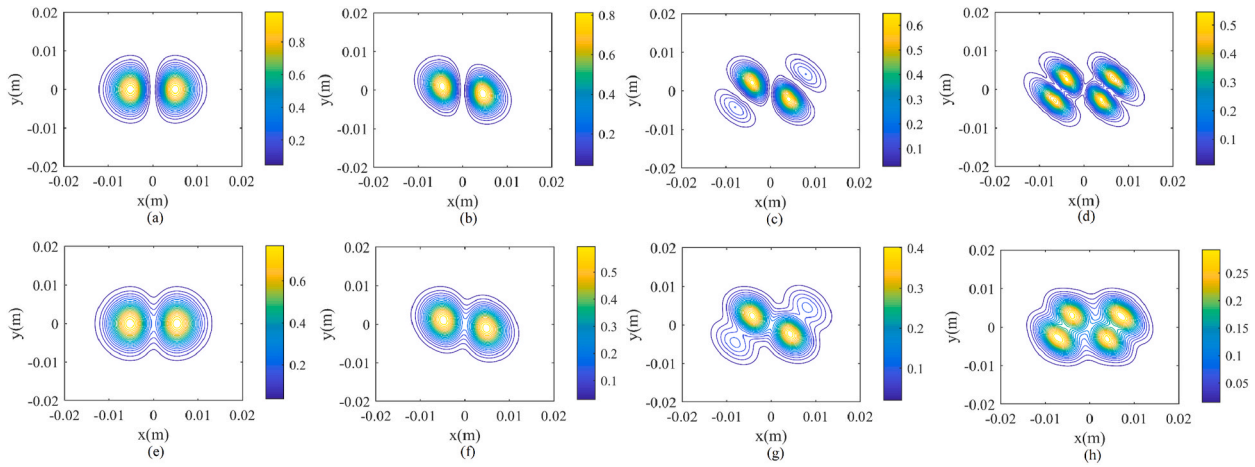

Fig. 4. Normalized intensity distribution of the Hermite-cosine-Gaussian rectangular multi-Gaussian correlated Schell-model beam in turbulent oceanic conditions with $n = 1$ and $m = 0$. The various parameters include: (a) $V_{xr} = 0\ m^{-1}$, $z = 10$ m, (b) $V_{xr} = 100\ m^{-1}$, $z = 10$ m, (c) $V_{xr} = 200\ m^{-1}$, $z = 10$ m, (d) $V_{xr} = 300\ m^{-1}$, $z = 10$ m, (e) $V_{xr} = 0\ m^{-1}$, $z = 50$ m, (f) $V_{xr} = 100\ m^{-1}$, $z = 50$ m, (g) $V_{xr} = 200\ m^{-1}$, $z = 50$ m, (h) $V_{xr} = 300\ m^{-1}$, $z = 50$ m.

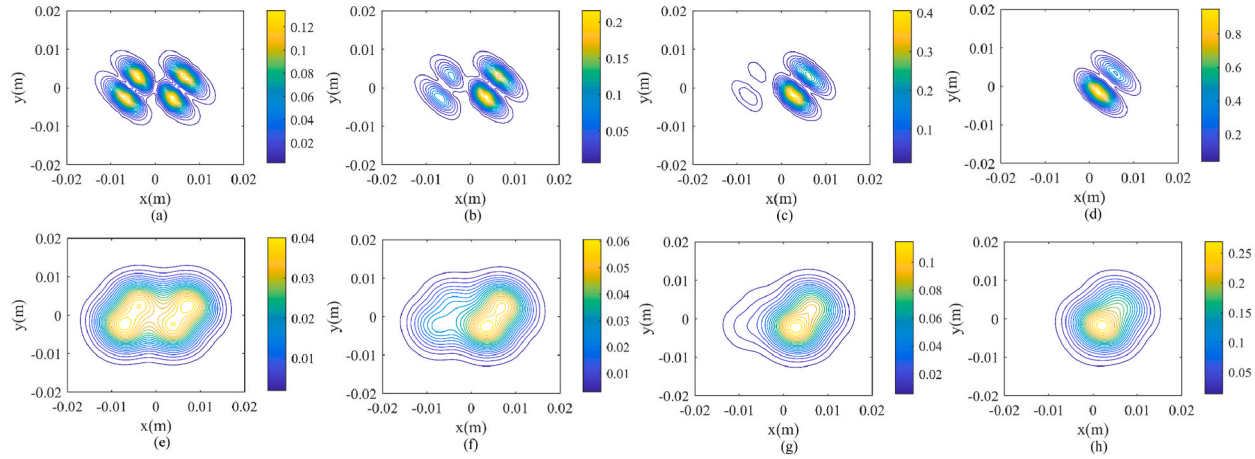

Fig. 5. Normalized intensity distribution of Hermite-cosine-Gaussian rectangular multi-Gaussian correlated Schell-model beam in oceanic turbulence with n = 1 and m = 0. The various parameters include: (a) $b_x = 0$, z = 10 m, (b) $b_x = 0.02$, z = 10 m, (c) $b_x = 0.05$, z = 10 m, (d) $b_x = 0.1$ z = 10 m. (e) $b_x = 0$, z = 80 m, (f) $b_x = 0.02$, z = 80 m, (g) $b_x = 0.05$, z = 80 m, (h) $b_x = 0.1$ z = 80 m.

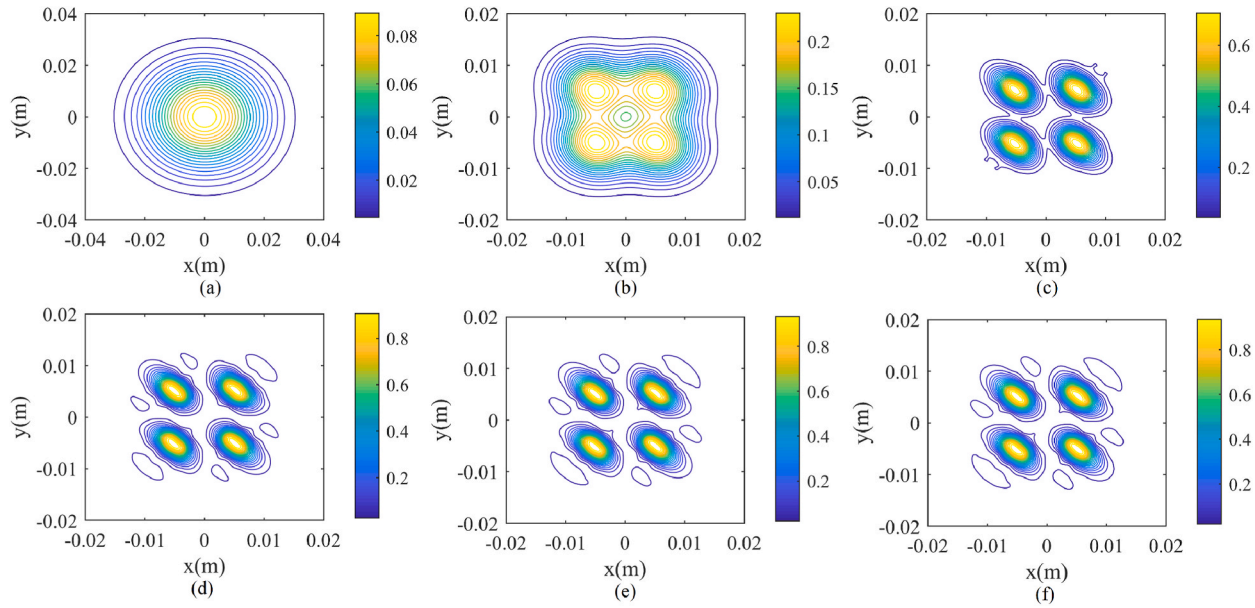

Fig. 6. Normalized intensity distribution of Hermite-cosine-Gaussian rectangular multi-Gaussian correlated Schell-model beam in oceanic turbulence with n = 1 and m = 1. The various parameters include: (a) $\chi_T = 10^{-4}\ k^2/s$, (b) $\chi_T = 10^{-5}\ k^2/s$, (c) $\chi_T = 10^{-6}\ k^2/s$, (d) $\chi_T = 10^{-7}\ k^2/\ s$, (e) $\chi_T = 10^{-8}\ k^2/s$, (f) $\chi_T = 10^{-9}\ k^2/s$.

affected by the changes in ocean turbulence parameters. Fig. 6 displays the normalized intensity under various mean square temperature dissipation rates, ranging from $10^{-4}\mathrm{k}^2/\mathrm{s}$ to $10^{-9}\mathrm{k}^2/\mathrm{s}$. As depicted in Fig. 6(a)-6(f), as the mean square temperature dissipation rate decreases, the normalized intensity converts from a single lobe profile to four three-lobe profiles, with energy dispersing from the center to the four side lobes. Furthermore, the normalized intensity of the HcosG rectangular multi-Gaussian correlated Schell-model beam increases, and the diffusion rate of the normalized intensity plot increases as the mean square temperature dissipation rate decreases.

Fig. 7(a)-7(c) illustrate the root-mean-square wavefront width of a Hermite-cosine-Gaussian multiple Gaussian correlated Schell-model beam with varying χ_T, ε, and ζ. As evident from the plots, all the curves exhibit a monotonic increase, with the slope of the curves increasing with the propagation distance. The difference between the curves in the near-field is smaller than that in the far-field. Furthermore, at the same propagation distance, the root-mean-square wavefront width increases with an increase in χ_T and ζ, and a decrease in ε.

Fig. 8 portrays the changes in the spectral coherence of the Hermite-Cosine-Gaussian rectangular multi-Gaussian correlated Schell-

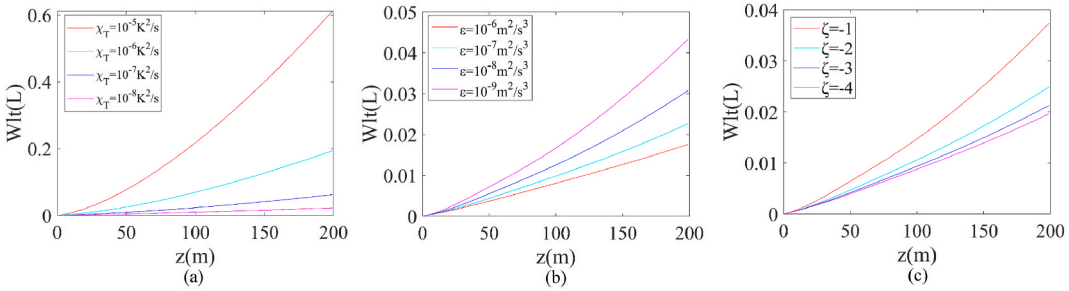

Fig. 7. Rms beam width of Hermite-cosine-Gaussian rectangular multi-Gaussian correlated Schell-model beam with (a) $\varepsilon = 10^{-7}\ m^2/\ s^3$, $\zeta = -2.5$ and different χ_T, (b) $\chi_T = 10^{-8}\ k^2/s$, $\zeta = -2.5$, and different ε, (c) $\chi_T = 10^{-8}\ k^2/s$, $\varepsilon = 10^{-7}\ m^2/s^3$, and different ζ.

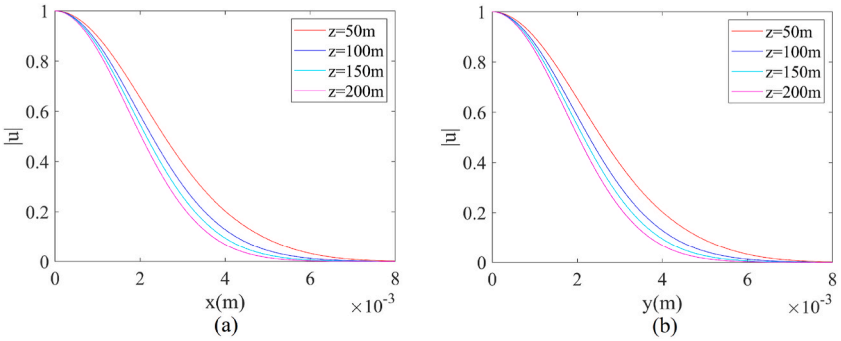

Fig. 8. The degree of coherence for Hermite-cosine-Gaussian rectangular multi-Gaussian correlated Schell-model beam propagating in oceanic turbulence as the function of (a) x and (b) y.

model beam in oceanic turbulence as a function of propagation distance. As evident from Fig. 8(a)-8(b), an increase in propagation distance results in a steeper coherence curve and a higher rate of spectral coherence attenuation. Additionally, it can be observed that as z increases, the differences in the curves become gradually smaller. Finally, a comparison between Figs. (8a) and (8b) reveals that the coherence curves are similar along the x-axis and y-axis.

4. Conclusion

Taking the HcosG rectangular multi-Gaussian Schell-model beam as an example, the average intensity, root-mean-square (RMS) wave number width, and coherence properties of the beam in oceanic turbulence are studied in this paper.

The results reveal that within a short propagation distance, the HcosG rectangular multi-Gaussian Schell-model beam exhibits a multi-lobe pattern, and the quantity, shape, and evolution behavior of the lobes depend on the beam parameters. The larger the V_{xr}, α_{sx}, α_{sy}, m, and n are, the larger the lobe number is. The larger α_{sx}, α_{sy} are, the faster these lobes merge in propagation. And the b_x controls the centroid positions of the lobes before merging.

The far-field patterns of the HcosG rectangular multi-Gaussian Schell-model beams in oceanic turbulence are always Gaussian-like. In the far field, the maximum intensity is also related to b_x, m, n, χ_T, α_{sx} and α_{sy}. Larger maximum intensity corresponds to larger b_x, α_{sx} and α_{sy}, and smaller χ_T, n and m.

As z increases, the spectral coherence decreases, and the differences between the spectral coherence curves become gradually smaller. For HcosG rectangular multi-Gaussian correlated Schell-model beams, better propagation performance was found in oceanic turbulence with larger χ_T, smaller ε, and larger ζ. The influence of these parameters on the rms beam width is more apparent in the far field than in the near field.

Author contribution statement

Xu Wu: Conceived and designed the experiments; Contributed reagents, materials, analysis tools or data; Wrote the paper.
Chuang Wang; Yuhui Kong; Kenan Wu: Performed the experiments; Analyzed and interpreted the data.

Data availability statement

No data was used for the research described in the article.

Additional information

No additional information is available for this paper.

Funding statement

Kenan Wu was supported by National Natural Science Foundation of China [61875197 & 61205139], Youth Innovation Promotion Association of the Chinese Academy of Sciences [2016168].

Declaration of competing interest

The authors declare that they have no known competing financial interests or personal relationships that could have appeared to influence the work reported in this paper.

References

[1] W. Fu, H. Zhang, Propagation properties of partially coherent radially polarized doughnut beam in turbulent ocean, Opt Commun. 304 (2013) 11–18, https://doi.org/10.1016/j.optcom.2013.03.029.
[2] D. Liu, Y. Wang, H. Yin, Evolution properties of partially coherent flat-topped vortex hollow beam in oceanic turbulence, Appl. Opt. 54 (2015) 10510–10516, https://doi.org/10.1364/AO.54.010510.
[3] D.J. Liu, Y.C. Wang, Properties of a random electromagnetic multi-Gaussian Schell-model vortex beam in oceanic turbulence, Appl. Phys. B 124 (2018) 1–9, https://doi.org/10.1007/s00340-018-7048-0.
[4] D.J. Liu, G.Q. Wang, Y.C. Wang, Average intensity and coherence properties of a partially coherent Lorentz-Gauss beam propagating through oceanic turbulence, Opt Laser. Technol. 98 (2018) 309–317, https://doi.org/10.1016/j.optlastec.2017.08.011.
[5] W.Y. Fu, H.M. Zhang, Polarization changes in a partially coherent radially polarized doughnut beam through turbulent ocean, J. Mod. Opt. 60 (18/19) (2013) 1576–1584, https://doi.org/10.1080/09500340.2013.844280.
[6] L.W. Casperson, A.A. Tovar, Hermite-sinusoidal-Gaussian beams in complex optical systems, J. Opt. Soc. Am. A 15 (4/6) (1998) 954–961, https://doi.org/10.1364/JOSAA.15.000954.
[7] A.E. Siegman, Hermite–Gaussian functions of complex argument as optical-beam eigenfunctions, J. Opt. Soc. Am. 63 (9) (1973) 1093–1094, https://doi.org/10.1364/JOSA.63.001093.
[8] H.T. Eyyuboğlu, Hermite-cosine-Gaussian laser beam and its propagation characteristics in turbulent atmosphere, J. Opt. Soc. Am. A 22 (8) (2008) 1527–1535, https://doi.org/10.1364/JOSAA.22.001527.
[9] B. Tang, Hermite-cosine-Gaussian beams propagating in uniaxial crystals orthogonal to the optical axis, J. Opt. Soc. Am. A 26 (12) (2009) 2480–2487, https://doi.org/10.1364/JOSAA.26.002480.
[10] Y. Baykal, Formulation of correlations for general-type beams in atmospheric turbulence 23 (4) (2006) 889–893, https://doi.org/10.1364/JOSAA.23.000889.
[11] N.R. Zhou, G.H. Zeng, Propagation properties of Hermite-cosine-Gaussian beams through a paraxial optical ABCD system with hard-edge aperture, Opt Commun. 232 (1–6) (2004) 49–59, https://doi.org/10.1016/j.optcom.2003.12.070.
[12] J. Li, Y.R. Chen, S.X. Xu, Y.Q. Wang, M.C. Zhou, Q. Zhao, Y. Xin, F.N. Chen, Analytical vectorial structure of Hermite-cosine-Gaussian beam in the far field, Opt Laser. Technol. 43 (2011) 152–157, https://doi.org/10.1016/j.optlastec.2010.06.005.
[13] J. Li, Z.J. Yang, Z.G. Pang, S.M. Zhang, Evolution characteristics of generalized Hermite-cosine-Gaussian solitons in optical nonlinear medium with spatial nonlocality, Results Phys. 37 (2022), 105490, https://doi.org/10.1016/j.rinp.2022.105490.
[14] Z. Hricha, M. Yaalou, A. Belafhal, Introduction of the vortex Hermite-Cosh-Gaussian beam and the analysis of its intensity pattern upon propagation, Opt. Quant. Electron. 53 (2021) 80, https://doi.org/10.1007/s11082-020-02665-2.
[15] J.H. Li, B.D. Lü, Propagation of Gaussian Schell-model vortex beams through atmospheric turbulence and evolution of coherent vortices, J. Opt. A: Pure Appl. Opt. 11 (4) (2009), 045710, https://doi.org/10.1088/1464-4258/11/4/045710, 1-045710:9.
[16] D.M. Deng, Propagation of elegant Hermite cosine Gaussian laser beams, Opt Commun. 259 (2) (2006) 409–414, https://doi.org/10.1016/j.optcom.2005.09.009.
[17] K.N. Wu, Y. Huai, T.L. Zhao, Y.Q. Jin, Propagation of partially coherent four-petal elliptic Gaussian vortex beams in atmospheric turbulence, Opt Express 26 (23) (2008) 30061–30075, https://doi.org/10.1364/OE.26.030061.
[18] M.J. Cheng, L.X. Guo, J.T. Li, X. Yan, K.J. Dong, Y. You, Average intensity and spreading of a radially polarized multi-Gaussian Schell-model beam in anisotropic turbulence, J. Quant. Spectrosc. Radiat. Transfer 218 (2018) 21812–21820, https://doi.org/10.1016/j.jqsrt.2018.06.024.
[19] X.L. Ma, D.J. Liu, Y.C. Wang, H.M. Yin, H.Y. Zhong, G.Q. Wang, Propagation of rectangular multi-Gaussian schell-model array beams through free space and non-Kolmogorov turbulence, Appl. Sci. 10 (2) (2020) 450, https://doi.org/10.3390/app10020450.
[20] Y. Dong, K.Y. Dong, S. Chang, Y.S. Song, Propagation of rectangular multi-Gaussian Schell-model vortex beams in turbulent atmosphere, Optik 207 (2020), 163809, https://doi.org/10.1016/j.ijleo.2019.163809.
[21] Y.K. Zhang, J. Wang, X.M. Qian, W.Y. Zhu, J.H. Li, Orbital angular momentum evolution of twisted multi-Gaussian Schell model beams in anisotropic turbulence, Opt Commun. 520 (2022), 128454, https://doi.org/10.1016/j.optcom.2022.128454.
[22] F. Gori, M. Santarsiero, Devising genuine spatial correlation functions, Opt. Lett. 32 (24) (2007) 3531–3533, https://doi.org/10.1364/OL.32.003531.
[23] Y. Huang, P. Huang, F. Wang, Z. Zhao, A. Zeng, The influence of oceanic turbulence on the beam quality parameters of partially coherent Hermite-Gaussian linear array beams, Opt Commun. 336 (2015) 146–152, https://doi.org/10.1016/j.optcom.2014.09.055.
[24] X.L. Ma, G.Q. Wang, H.Y. Zhong, Y.C. Wang, D.J. Liu, Propagation of a rectangular multi-Gaussian schell-model vortex beam in uniaxial crystal, Optik 221 (2020), 165318, https://doi.org/10.1016/j.ijleo.2020.165318.
[25] E. Wolf, Unified theory of coherence and polarization of random electromagnetic beams, Phys. Lett. 312 (2003) 263–267, https://doi.org/10.1016/S0375-9601(03)00684-4.
[26] O. Korotkova, Random sources for rectangular far fields, Opt. Lett. 39 (1) (2014) 64–67, https://doi.org/10.1364/OL.39.000064.
[27] B. Zhang, Y.P. Huang, Z.H. Gao, Z.C. Duan, G.P. Zhao, Evolution behavior of Gaussian Schell-model vortex beams propagating through oceanic turbulence, Opt Exp. 22 (15) (2014) 17723–17734, https://doi.org/10.1364/OE.22.017723.
[28] S.C.H. Wang, M.A. Plonus, Optical beam propagation for a partially coherent source in the turbulent atmosphere, J. Opt. Soc. Am. 69 (1979) 1297–1304, https://doi.org/10.1364/JOSA.69.001297.
[29] H.T. Eyyuboğlu, Y. Baykal, Analysis of reciprocity of cos-Gaussian and cosh-Gaussian laser beams in a turbulent atmosphere, Opt Exp. 12 (20) (2004) 4659–4674, https://doi.org/10.1364/OPEX.12.004659.
[30] Y.M. Dong, L.N. Guo, C.H. Liang, F. Wang, Y.J. Cai, Statistical properties of a partially coherent cylindrical vector beam in oceanic turbulence, J. Opt. Soc. Am. A 32 (5) (2015) 894–901, https://doi.org/10.1364/JOSAA.32.000894.

[31] D.J. Liu, L. Chen, Y.C. Wang, G.Q. Wang, H.M. Yin, Average intensity properties of flat-topped vortex hollow beam propagation through oceanic turbulence, Optik 127 (17) (2016) 6961–6969, https://doi.org/10.1016/j.ijleo.2016.04.142.
[32] J. Xu, D.M. Zhao, Propagation of a stochastic electromagnetic vortex beam in the oceanic turbulence, Opt Laser. Technol. 57 (2014) 189–193, https://doi.org/10.1016/j.optlastec.2013.10.019.
[33] T. Shirai, A. Dogariu, E. Wolf, Directionality of Gaussian Schell-model beams propagating in atmospheric turbulence, Opt. Lett. 28 (8) (2003) 610–612, https://doi.org/10.1364/OL.28.000610.